# Characterization and Simulation of Nanoscale Catastrophic Failure of Metal/Ceramic Interfaces

Xueqiong Fu, Lihong Liang,* and Yueguang Wei*

Cite This: *ACS Omega* 2023, 8, 20313−20322

Read Online

ACCESS | 📊 Metrics & More | 📰 Article Recommendations

**ABSTRACT:** The catastrophic failure of metal/ceramic interfaces is a complex process involving the energy transfer between accumulated elastic strain energy and many types of energy dissipation. To quantify the contribution of bulk and interface cohesive energy to the interface cleavage fracture without global plastic deformation, we characterized the quasi-static fracture process of both coherent and semi-coherent fcc-metal/MgO(001) interface systems using a spring series model and molecular static simulations. Our results show that the theoretical catastrophe point and spring-back length by the spring series model are basically



consistent with the simulation results of the coherent interface systems. For defect interfaces with misfit dislocations, atomistic simulations revealed an obvious interface weakening effect in terms of reduced tensile strength and work of adhesion. As the model thickness increases, the tensile failure behaviors show significant scale effects—thick models tend to catastrophic failure with abrupt stress drop and obvious spring-back phenomenon. This work provides insight into the origin of catastrophic failure at metal/ceramic interfaces, which highlights a pathway by combining the material and structure design to improve the reliability of layered metal–ceramic composites.
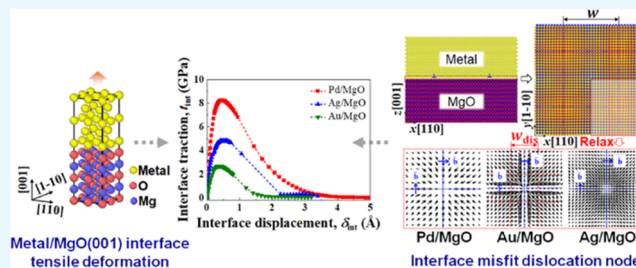
## 1. INTRODUCTION

Layered metal−ceramic composites, which integrate the advantages of metal (e.g., ductility, electrical conductivity) and ceramics (e.g., high strength, chemical resistance), are key to many technological applications such as electronic devices,[1−3] thermal barrier coatings (TBC),[4−6] and semiconductors.[7,8] The metal/ceramic interface is a crucial component of layered metal−ceramic composites, and the adhesion of this interface plays a pivotal role in dominating the mechanical, thermal, and electrical properties of the composites.[9] Because of differences in the lattice structure and properties (e.g., Young's modulus, coefficient of thermal expansion (CTE)) between metals and ceramics, defects such as misfit dislocations appear at the interface, weakening the interface bonding and decreasing the effective interface area.[10] At a low temperature or at a high loading rate, cleavage fracture without or with little global plastic deformation often happens at the interface.[11] This interface failure, which arises suddenly and catastrophically, often stems from atomic bond breaking near the crack tip and may lead to the breakdown of related structures and devices. Therefore, it is necessary to investigate the mechanisms of cleavage fracture of metal/ceramic interfaces and analyze the effects of defects on interface microstructures and fracture behaviors at atomic levels.

Interface fracture is a complex process involving the energy transfer between elastic strain energy stored in bulk materials and many types of energy dissipation such as surface energy and plastic work.[12−14] For the case of cleavage fracture, the driving force for crack extension is the difference between the accumulated elastic strain energy and the energy needed to create new surfaces of the crack. Based on the assumption in phenomenological fracture mechanics to separate the elastic strain energy into bulk and cohesive parts,[15] a one-dimensional elastic model has been proposed to describe both macrocracks and microcracks forming a so-called process zone.[16−18] Instead of considering the full relaxation of a cohesive potential, Nguyen et al.[16] sought energy minimization of large—but finite—collections of interatomic planes and found a universal form of the macroscopic cohesive law. However, because of the mathematical complexity, most theoretical models deal with the fracture of homogeneous materials. For interface systems made of two dissimilar materials, the interface can be considered as a natural material discontinuity where cracking usually happens, and three materials (if the interface can also be regarded as a kind of material) with different interplanar interactions need to be described.
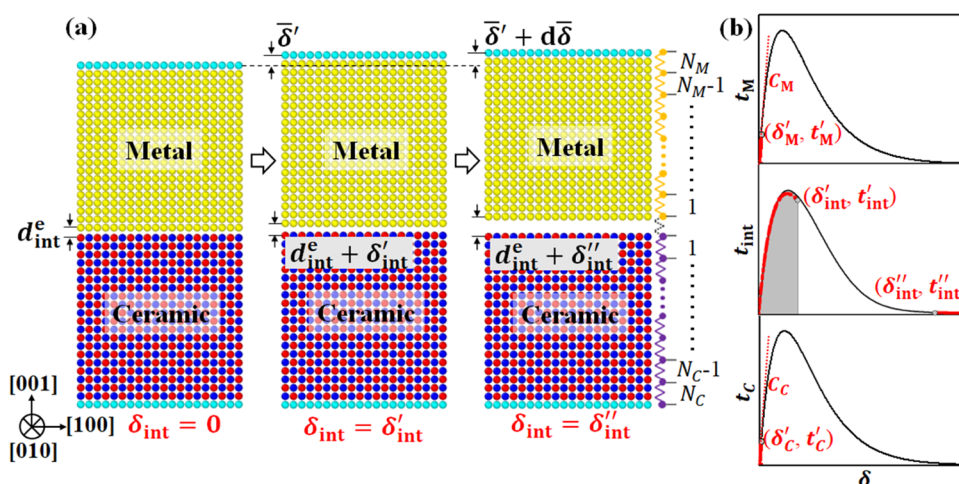
**Figure 1.** (a) Schematics of atomistic scale interface fracture in a layered structure of fcc-metal/MgO. $\delta_{int} = 0$: initial equilibrium state. $\delta_{int} = \delta'_{int}$: catastrophe point before interface catastrophic failure. $\delta_{int} = \delta''_{int}$: spring-back point after interface catastrophic failure. (b) Interplanar cohesive relationships of the metal, interface, and ceramic (from top to bottom). Rigid tension results (black lines) and relaxed tension results (red dots).

In this paper, our focus is to explore the effect of the bulk material, interface structure, and interface cohesive relationships on the mode I cleavage fracture of metal/ceramic interfaces, especially the fracture criterion and scale effects. Compared with mode II and mode III fracture, a crack front in a solid after propagation tries to reach mode I loading conditions regardless of external loading.[19] A spring series model based on energy analysis was proposed to characterize the interface catastrophic failure and quantify the energy transfer between bulk energy and interface cohesive energy during interface fracture. To validate the catastrophe point and spring-back point representing the start and end of catastrophic failure, we carried out molecular static simulations of the quasi-static fracture of metal/ceramic interfaces. The fcc-metal/MgO(001) interfaces, which widely exist in advanced engineering applications[20−22] and have been model metal/ceramic interfaces for their simplicity,[10,23,24] were chosen as examples in the numerical models. Through comparison between coherent and semi-coherent interfaces, we investigated the interface weakening effect caused by misfit dislocations in terms of interface strength and fracture behaviors.

## 2. SPRING SERIES MODEL

For the mode-I fracture of metal/ceramic interface systems at zero temperature, the total energy $\bar{\Phi}$ consists of three parts

$$\bar{\Phi}(\bar{\delta}) = \sum_{i=1}^{N_M} \Phi_M(\delta_i) + \sum_{i=1}^{N_C} \Phi_C(\delta_i) + \Phi_{int}(\delta_{int}) \tag{1}$$

where $\Phi_M$, $\Phi_C$, and $\Phi_{int}$ denote the interplanar cohesive energies of the metal, ceramic, and interface, respectively. $N_M$ and $N_C$ denote the numbers of interatomic planes in the metal and ceramic. The boundary displacement $\bar{\delta}$ equals the sum of all interplanar opening displacements

$$\bar{\delta} = \sum_{i=1}^{N_M} \delta_i + \sum_{i=1}^{N_C} \delta_i + \delta_{int} \tag{2}$$

During the quasi-static deformation process, each part of the interface system satisfies the force equilibrium condition, i.e., the interplanar cohesive tractions equal the far-field cohesive traction $\bar{t}$:

$$t_M(\delta_M) = t_C(\delta_C) = t_{int}(\delta_{int}) = \bar{t}(\bar{\delta}) \tag{3}$$

Equations 1−3 are the governing equations of the heterogeneous interface fracture model.

As depicted schematically in Figure 1, if each atomic layer is equivalent to a material point, then the interface model can be discretized to many spaced material points interacting through an array of springs connecting neighboring points, i.e., the spring series model. According to the energy change of the interface system, the interface fracture process can be divided into two stages: the loading stage $(\delta_{int} \leq \delta'_{int})$ and the catastrophic failure stage $(\delta'_{int} < \delta_{int} \leq \delta''_{int})$. In the loading stage, external work is transformed into the elastic energy accumulated in bulk materials and interfacial cohesive energy. When the total energy of the interface system reaches the maximum, i.e., a further increase in boundary displacement will cause the interface to enter the fast-softening section of the interface cohesive curve, the interface loses its bearing capacity and enters the catastrophic failure stage.

**2.1. Catastrophe Point ($\delta'_{int}$, $t'_{int}$).** For macroscopic interface systems $(N_M \to \infty, N_C \to \infty)$, the interplanar opening displacements in bulk materials tend to zero under finite boundary displacement; thus, the interplanar interactions can be modeled as linear springs with stiffness $C$.[16] At the interface, the interplanar traction−separation relationship is usually nonlinear. We express the interface cohesive energy $\Phi_{int}$ as the integral of the interface traction $t_{int}$. According to the theoretical model in ref 25, the total energy $\bar{\Phi}$ in eq 1 can be written as

$$\bar{\Phi} = N_M \frac{C_M}{2} \delta_M^2 + N_C \frac{C_C}{2} \delta_C^2 + \int_0^{\delta_{int}} t_{int}\, d\delta_{int} \tag{4}$$

The force equilibrium equation eq 3 can be substituted into eq 4 and $\bar{\Phi}$ can be written as a function of the interface opening displacement $\delta_{int}$

$$\bar{\Phi}(\delta_{int}) = N_M \frac{C_M}{2}\left(\frac{t_{int}}{C_M}\right)^2 + N_C \frac{C_C}{2}\left(\frac{t_{int}}{C_C}\right)^2 + \int_0^{\delta_{int}} t_{int}\, d\delta_{int} \tag{5}$$

At the catastrophe point, the total energy $\bar{\Phi}$ reaches the maximum and its first derivative equals zero
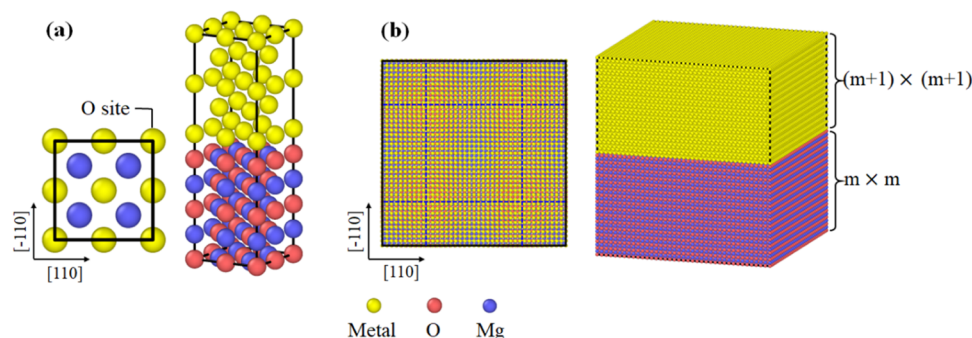
**Figure 2.** Fcc-metal/MgO(001) interface model: (a) coherent interface and (b) semi-coherent interface.

$$\frac{d\overline{\Phi}(\delta_{int})}{d\delta_{int}} = 0 \rightarrow \left( \frac{N_M}{C_M} \frac{dt_{int}}{d\delta_{int}} + \frac{N_C}{C_C} \frac{dt_{int}}{d\delta_{int}} + 1 \right) t_{int} = 0 \tag{6}$$

Note that interplanar traction $t_{int} > 0$ at the catastrophe point; then, one can derive the slope of the interface cohesive curve at the catastrophe point

$$\frac{dt_{int}}{d\delta_{int}}\Big|_{\delta_{int}=\delta_{int}'} = -\frac{C_M C_C}{N_M C_C + N_C C_M} < 0 \tag{7}$$

It is interesting that the interfacial catastrophic failure does not occur at the peak interface traction but somewhere after it. When the interface system contains a sufficiently large number of atomic layers ($N_C \rightarrow \infty$, $N_M \rightarrow \infty$), $\frac{dt_{int}}{d\delta_{int}}\Big|_{\delta_{int}=\delta_{int}^c} \rightarrow 0$, i.e., the catastrophe point coincides with the peak interface traction point.

**2.2. Spring-back Point ($\delta_{int}''$, $t_{int}''$).** Considering the discontinuities in most material properties (e.g., thermal and elastic properties) across metal/ceramic interfaces, the interface is often the weak link in the system[13,26] and failure usually occurs at the interface. Therefore, we consider interface fracture in the model. At the catastrophe point, the interface cohesive relationship enters the softening stage, and the corresponding boundary displacement $\overline{\delta}'$ is

$$\overline{\delta}' = N_M \frac{t_{int}'}{C_M} + N_C \frac{t_{int}'}{C_C} + \delta_{int}' \tag{8}$$

With a slight increase in $\overline{\delta}$, the interface loses its bearing capacity and a fracture zone appears. The bulk materials are unloaded as this damage increases, accompanied by rapid release of elastic energy and interface spring-back (Figure 1a)

$$\overline{\delta}' + d\overline{\delta} = N_M \frac{t_{int}''}{C_M} + N_C \frac{t_{int}''}{C_C} + \delta_{int}'' \tag{9}$$

Evidently, in the limit of $d\overline{\delta} \rightarrow 0$, the spring-back length $\Delta\delta_{int}$ after interface catastrophic failure reduces to

$$\delta_{int}'' - \delta_{int}' \sim \left( N_M \frac{t_{int}' - t_{int}''}{C_M} + N_C \frac{t_{int}' - t_{int}''}{C_C} \right) \text{ as } d\overline{\delta} \rightarrow 0 \tag{10}$$

After the interface spring-back, the interface breaks suddenly and the interface traction decreases from $t_{int}'$ to $t_{int}''$. Since the total energy of the interface system decreases with the decrease of interface traction (eq 5), the reduction of $t_{int}$ during interfacial fracture is accompanied by the release of system energy. Note that the spring-back length $\Delta\delta_{int}$ is proportional to the decrease

of interface traction ($t_{int}' - t_{int}''$) after interface breaking, which corresponds to the sudden release of elastic energy. Therefore, the spring-back length $\Delta\delta_{int}$ characterizes the energy release rate during interfacial fracture to some extent. For an interface system with a fixed thickness ratio, the thicker the interface model, the longer the spring-back length.

## 3. ATOMISTIC SIMULATION METHOD

**3.1. Interface Model.** As illustrative examples, we considered three fcc-metal/MgO(001) interface systems: Pd/MgO, Ag/MgO, and Au/MgO. Because of the lattice mismatch, equilibrium fcc-metal/MgO(001) interfaces are usually semi-coherent with ordered, localized interfacial misfit dislocations.[27,28] In the region between the misfit dislocation lines, metal atoms match perfectly with MgO atoms, forming a local interfacial coherent region. In this work, both coherent and semi-coherent metal/MgO(001) interface models were constructed (Figure 2). The cubic axis of fcc-metal and rock-salt structure MgO were aligned, i.e., $[110]_M\|[110]_{MgO}$ ($x$-axis), $[\overline{1}10]_M\|[\overline{1}10]_{MgO}$ ($y$-axis), and $[001]_M\|[001]_{MgO}$ ($z$-axis). The interface normal was parallel to the $[001]$ crystal orientation, in accordance with the interface orientation relationship in experiments.[27,29,30]

In the coherent interface models, metal atoms sit on the most stable O sites.[31−33] In the semi-coherent interface models, the number of unit cells parallel to the interface was set as $(m + 1) \times (m + 1)$: $m \times m$. Two groups of mutually perpendicular dislocation lines (DLs) were placed in the metal side (marked by the blue dashed lines in Figure 2b). According to the lattice mismatch, the ratios of unit cells between metal and MgO were 14:13 (Pd/MgO), 20:19 (Ag/MgO), and 26:25 (Au/MgO). The interface model was periodic in $x$, $y$, and $z$ directions. To avoid spurious slab−slab interactions caused by the periodic boundary condition along the $z$ direction, the metal slab and MgO slab were separated by a vacuum region, which was twice the thickness of the interface system. The interatomic interactions were described by the Rahman−Stillinger−Lemberg pair potential extracted directly from ab initio adhesive or cohesive energies.[34] These potentials have proven to be able to reproduce the basic elastic and energetic properties of bulk materials, as well as the adhesive energies of metal/ceramic interfaces.[3,35,36]

**3.2. Rigid-type Fracture Simulation.** Rigid-type fracture simulations were conducted to obtain the interplanar cohesive relationships. For both coherent interface models and bulk material models, the models were first relaxed via the conjugate gradient (CG) algorithm. Then, the upper and lower parts of the models were totally fixed, and the two parts were rigidly separated along the $[001]$ direction. The energy and interplanar
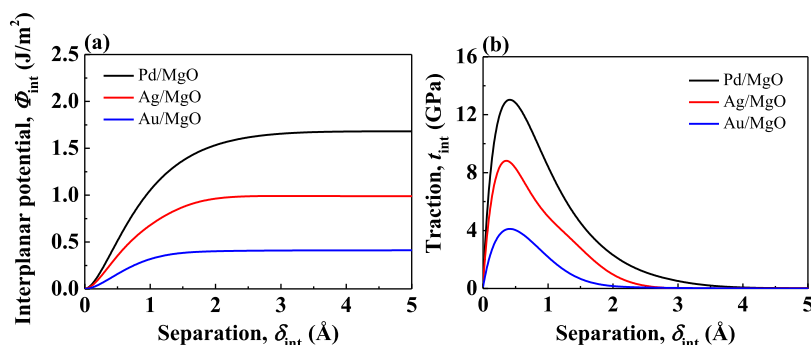
**Figure 3.** (a) Interplanar potentials and (b) traction−separation relationships of three metal/MgO interfaces.
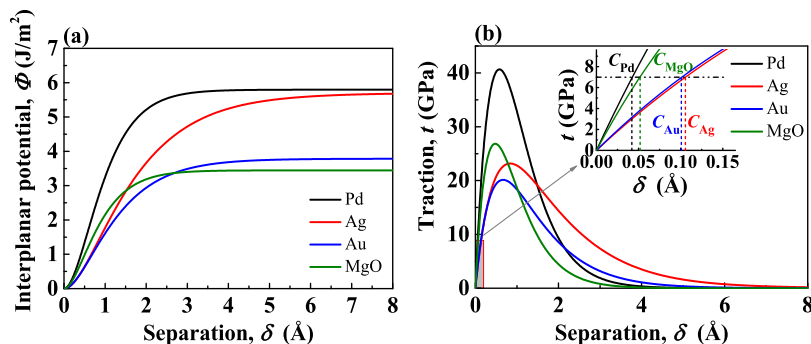


**Figure 4.** (a) Interplanar potentials and (b) traction−separation relationships of bulk materials.

traction during rigid-type fracture were recorded to obtain the intrinsic interplanar potentials and traction−separation relationships.

**3.3. Quasi-static Fracture Simulation.** The initial coherent and semi-coherent interface models were relaxed through two molecular static methods—the FIRE algorithm and the conjugate gradient (CG) algorithm with a force convergence tolerance of $10^{-4}$ eV/Å. Then, the bottom monolayer (ML) was fixed, and the top ML was iteratively displaced along the [001] direction with a step size of 0.01 Å. Further check shows that 0.01 Å is small enough to capture the breaking of metal−O bonds at the interface. After each displacement loading, the mobile atoms between boundaries were equilibrated through the CG algorithm under interatomic potentials. To study the change of interface interaction and system energy in the process of catastrophic failure, we transformed from boundary displacement loading to interface displacement loading at the catastrophe point: the boundary monolayers (MLs) were fixed while the interfacial metal ML and MgO ML were separated in a displacement ratio inversely proportional to the ratio of spring stiffness. This ensures that the interface system satisfies the force equilibrium condition throughout the simulation. During the process of tensile deformation, there is only normal relative displacement between adjacent atomic layers and the shear stress in the material is zero. Therefore, the phase angle of loading is zero. The simulations were performed using LAMMPS.[37]

## 4. RESULTS

**4.1. Interplanar Potentials.** Figures 3 and 4 show the interplanar potentials and traction−separation relationships for interfaces and bulk materials obtained by the rigid-type fracture simulation. For all metal/MgO(100) interfaces, the interplanar potential energies increase with the increase of interface distance

and remain constant after the interface is completely separated (Figure 3a). The interface traction−separation relationships were obtained by differentiating the potential energy with respect to the interface distance. Interface traction $t_{int}$ increases monotonically from zero to the peak value $t_{int}^{max}$. Then, the interface traction curve enters the softening stage and $t_{int}$ decreases slowly with the increase of interface separation distance (Figure 3b). Among the three fcc-metal/MgO interfaces, the Pd/MgO interface with the highest strength (13.03 GPa) and interfacial separation energy $E_{sep}$ (1.68 J/m²) is relatively strong. This is partly due to the relatively small electron transfer at the Pd/MgO(100) interface, so the cohesion of the metal is expected to be little modified by the MgO.[33]

For bulk materials, the interplanar potential energies increase with the increase of interplanar separation distance and remain constant after the bulk materials are completely separated to form two new free surfaces (Figure 4a). The shape of interplanar traction−separation curves of bulk materials (Figure 4b) is similar to that of the interfaces (Figure 3b). However, the interplanar strengths are much higher than the interface strengths, indicating that interface fracture rather than bulk material fracture is energetically favorable. This reflects the weak link characteristics of the metal/ceramic interfaces.[13,26] The interplanar spring stiffnesses $C$ of bulk materials are obtained from the slope of the initial linear segment of the $t-\delta$ curve, as listed in Table 1. To verify the values of the interplanar spring stiffness $C$, the calculated $C$ values were compared with the elastic constant $C_{11}$, which measures the ability of a material to resist uniaxial tension or compression and is equivalent to the stiffness of an ordinary spring. For Ag and Au, the interplanar spring stiffness $C$ values are nearly one-half of that of MgO. While for Pd, which has a higher elastic constant than Ag and Au, the interplanar spring stiffness $C$ is close to that of MgO.[38] For

**Table 1. Interplanar Spring Stiffnesses $C$ and Elastic Constants $C_{11}$ of Bulk Materials in the Metal/MgO Interface Systems**

| bulk materials | $C$ (GPa/Å) | $C_{11}$ (GPa) |
|---|---|---|
| Pd | 162.31 | 227.1[38] |
| Ag | 65.12 | 122.2[38] |
| Au | 68.15 | 192.9[38] |
| MgO | 137.26 | 294[38] |

different bulk materials, the relative value of $C$ is basically consistent with that of $C_{11}$.

The difference in interplanar spring stiffnesses and elastic constants between the metal (Pd, Ag, and Au) and MgO indicates an elastic mismatch between metal and MgO. For an interface between two elastic materials, the fracture behavior depends on the elastic mismatch. Dundurs' parameters $\alpha$ and $\beta$ have been proven useful in characterizing the elastic mismatch of bimaterials[39−41] and the parameters are[42]

$$\alpha = \frac{\mu_1(\kappa_2 + 1) - \mu_2(\kappa_1 + 1)}{\mu_1(\kappa_2 + 1) + \mu_2(\kappa_1 + 1)},$$

$$\beta = \frac{\mu_1(\kappa_2 - 1) - \mu_2(\kappa_1 - 1)}{\mu_1(\kappa_2 + 1) + \mu_2(\kappa_1 + 1)} \quad (11)$$

where $\mu_i$ is the shear modulus, the constant $\kappa_i = 3 - 4\nu_i$ for plane strain and $\kappa_i = (3 - \nu_i)/(1 + \nu_i)$ for plane stress, where $\nu_i$ denotes Poisson's ratio. Subscripts 1 and 2 denote the two materials. The Durdurs' parameters for the considered combinations of metal and ceramic are shown in Table 2. $\alpha$ is a measure of the relative

**Table 2. Durdurs' Parameters $\alpha$ and $\beta$ for the Combinations of Metal and Ceramic**

| material 1/material 2 | $G_1/G_2$ | $\alpha$ | $\beta$ |
|---|---|---|---|
| Pd/MgO | 0.416 | −0.39 | −0.059 |
| Ag/MgO | 0.275 | −0.56 | −0.102 |
| Au/MgO | 0.269 | −0.54 | −0.056 |

stiffness of the two materials and a negative value of $\alpha$ means that material 1 is relatively soft and material 2 is relatively rigid. Note that for the Ag/MgO interface, the absolute value of $\alpha$ is the largest, indicating that the stiffness difference between Ag and MgO is the most significant.

**4.2. Interface Catastrophic Failure Behavior.** *4.2.1. Coherent Interface.* Figure 5 shows the catastrophic failure

behaviors of three coherent metal/MgO(001) interfaces by the quasi-static fracture simulation. As predicted by eq 7, the catastrophe points of different interface models all fall behind the peak interface tractions. Equation 7 also indicates that the higher the interplanar stiffness of metal, the greater the magnitude of the slope corresponding to the catastrophe point, meaning that the catastrophe point is further away from the peak point of interface stress where the slope is zero. Among the three metals studied in this work, Pd has the highest interplanar spring stiffness $C$, so the catastrophe point of the Pd/MgO interface is farther from the peak point of interface stress. Though the interplanar spring stiffnesses of Ag and Au are basically the same, the strength of the Ag/MgO interface is higher than that of the Au/MgO interface, which makes the interface traction−separation curve of the Ag/MgO interface steeper. Consequently, the catastrophe point determined using eq 7 is close to the peak interface stress.

Based on eqs 7 and 10 and Table 1, one can calculate the interface displacement after interface spring-back $\delta''_{int}$. Figure 5a shows that the simulation results of $\delta''_{int}$ (marked by solid arrows) of the Pd/MgO interface and the Au/MgO interface agree well with the theoretical results (marked by dotted arrows). For the Ag/MgO interface, the simulation result is obviously larger than the theoretical result. Since Ag is soft and the interface strength is relatively high, the Ag/MgO interface system has the greatest elastic elongation at the catastrophe point. Consequently, the boundary effect in molecular simulations—larger interlayer spacing in the metal near the fixed boundary and the interface[43]—is evident.

*4.2.2. Semi-coherent Interface.* Figure 6 shows the disregistry plot of the equilibrium metal/MgO interfaces. After relaxation, the atomic displacements around the misfit dislocation lines, especially near the dislocation nodes, are the largest. The misfit dislocations are all edge type with the Burgers vector $\mathbf{b}$ = $a/2\langle110\rangle$.[30,44,45] Both interface interaction and stiffness of metal affect the equilibrium interface structure. Figure 6 shows that the atomic displacements around the misfit dislocation lines of the Ag/MgO interface are the most significant, indicating larger deformation of Ag near the interface after interface relaxation. While for the Au/MgO interface with lower interface strength than the Ag/MgO interface, the atomic displacements after interface relaxation are more evenly distributed. Earlier HRTEM images of the deposited Au clusters on MgO show a coherent interface configuration.[29]

The generation of misfit dislocations at the metal/ceramic interfaces affects the interfacial atomic configurations as well as
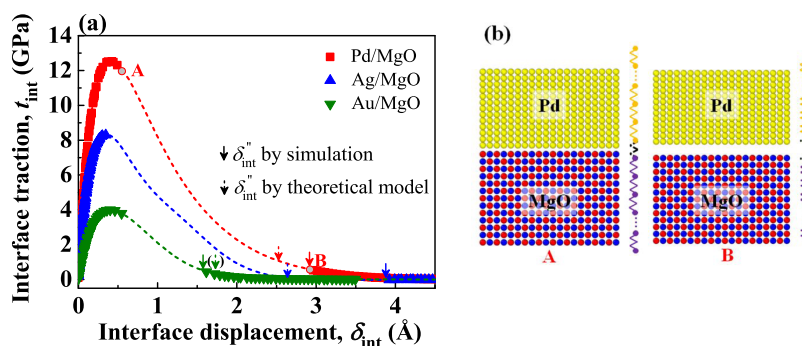


**Figure 5.** (a) Interface catastrophic failure behaviors of three coherent metal/MgO interfaces (6u−6u interface model). The solid arrows and dotted arrows mark the interface displacement $\delta''_{int}$ after spring-back by simulation and eqs 7 and 10. (b) The atomic configurations and schematics of spring series models corresponding to point A and point B in panel (a).
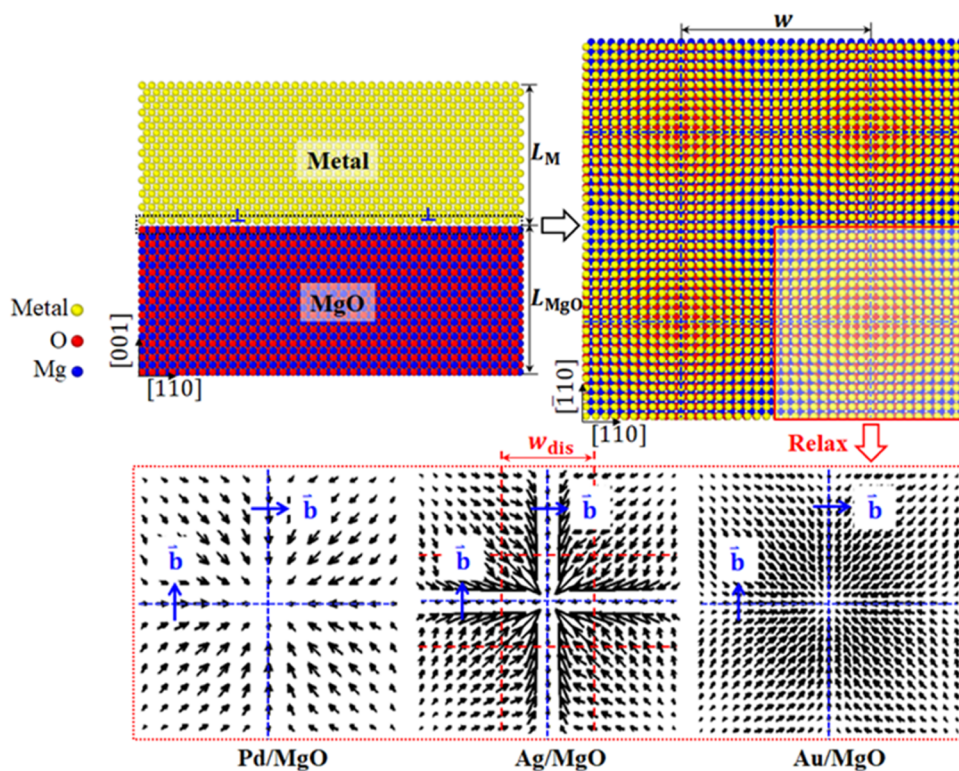
**Figure 6.** Disregistry plot of three semi-coherent metal/MgO interface systems showing the misfit dislocation network. For clarity, only one dislocation node is shown.

**Table 3. Comparison of Equilibrium Interface Distance $d_0$ and Work of Adhesion $W_{adh}$ between Coherent and Semi-coherent Metal/MgO Interfaces[a]**

|  |  | $d_0$ (Å) | | $W_{adh}$ (J/m$^2$) | | |
|---|---|---|---|---|---|---|
| interfaces |  | this work | exp. | this work | exp. | $w_{dis}/w$ |
| Pd/MgO | coherent | 2.21 | 2.22 ± 0.03[30] | 1.63 | — | 0.17 |
|  | semi-coherent | 2.24 | 2.15−2.23[30] | 1.28 |  |  |
| Ag/MgO | coherent | 2.39 | 2.52 ± 0.1[47] | 0.99 | 0.49−0.89[48] | 0.21 |
|  | semi-coherent | 2.42 |  | 0.62 | 0.45 ± 0.1[49] |  |
| Au/MgO | coherent | 2.65 | 2.97[29] | 0.40 | — | 0.16 |
|  | semi-coherent | 2.71 |  | 0.26 |  |  |

[a] $w_{dis}/w$: the dimensionless widths of misfit dislocations.
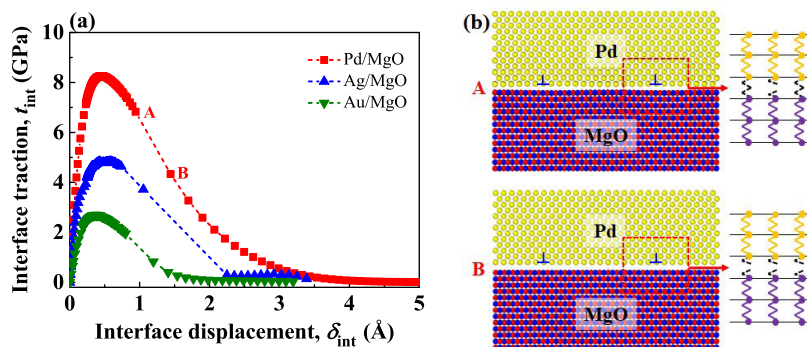


**Figure 7.** (a) Interface catastrophic failure behaviors of three semi-coherent metal/MgO interfaces (6u−6u interface model). (b) The atomic configurations and schematics of spring series models corresponding to point A and point B in panel (a).

the interface adhesion. Table 3 lists the equilibrium interface distance $d_0$ and work of adhesion $W_{adh}$ of both coherent and semi-coherent metal/MgO interfaces. As a measure of interface bond strength, $W_{adh}$ is obtained by subtraction of total energies

at equilibrium from slab energies at large interface separation.[46] Because of the greater metal−O distance around the misfit dislocations, the equilibrium interface distances of the three semi-coherent metal/MgO interfaces are larger than that of the
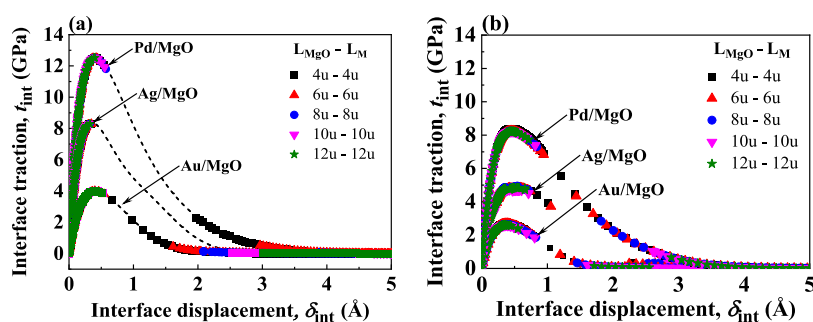
**Figure 8.** Interface traction−separation relationships of three metal/MgO interface systems with different thicknesses: (a) coherent interface and (b) semi-coherent interface.

**Table 4. Interface Displacement at the Catastrophe Point ($\delta'_{int}$) and the Spring-back Length ($\Delta\delta_{int}$) of the Pd/MgO Interface, Ag/MgO Interface, and Au/MgO Interface of Different Thicknesses**

| | | Pd/MgO | | Ag/MgO | | Au/MgO | |
|---|---|---|---|---|---|---|---|
| model thickness | | $\delta'_{int}$ (Å) | $\Delta\delta_{int}$ (Å) | $\delta'_{int}$ (Å) | $\Delta\delta_{int}$ (Å) | $\delta'_{int}$ (Å) | $\Delta\delta_{int}$ (Å) |
| 4u−4u | spring series model | 0.66 | 0.62 | 0.47 | 1.11 | — | — |
| | atomistic simulation | 0.57 | 1.39 | 0.36 | 2.42 | — | — |
| 6u−6u | spring series model | 0.55 | 1.82 | 0.42 | 2.35 | 0.66 | 0.69 |
| | atomistic simulation | 0.47 | 2.42 | 0.33 | 3.56 | 0.55 | 1.03 |
| 8u−8u | spring series model | 0.51 | 2.68 | 0.40 | 3.18 | 0.57 | 1.30 |
| | atomistic simulation | 0.49 | 3.25 | 0.32 | 4.70 | 0.53 | 1.61 |
| 10u−10u | spring series model | 0.49 | 3.44 | 0.39 | 4.00 | 0.54 | 1.73 |
| | atomistic simulation | 0.42 | 4.16 | 0.33 | 5.80 | 0.52 | 2.04 |
| 12u−12u | spring series model | 0.46 | 4.17 | 0.38 | 4.77 | 0.52 | 2.12 |
| | atomistic simulation | 0.43 | 5.08 | 0.33 | 6.97 | 0.53 | 2.53 |

coherent interfaces. Besides, misfit dislocations reduce the number of metal−O bonds that contribute to the adhesion of metal/MgO interfaces, so the $W_{adh}$ of the semi-coherent interface is lower than that of the corresponding coherent interface.

Figure 7 shows the interface catastrophic failure behaviors of three semi-coherent metal/MgO interfaces. Compared with the coherent interface systems of the same thickness, the interface fracture processes of semi-coherent interface systems appear to be more continuous: the catastrophe point is farther from the peak interface traction and the spring-back length is shorter (Figure 7a). This transition in fracture characteristics is closely associated with the inhomogeneous distribution of the metal−O bond distance at the semi-coherent metal/MgO interfaces. After $t_{int}$ reaches the peak value, the "weak" springs in the dislocation node regions first break, while the "strong" springs in the coherent regions remain connected (point A in Figure 7b). When all interfacial springs break, the interface enters the softening stage before complete separation (point B in Figure 7b). This gradual breaking of interface springs results in a slower energy release rate during the process of interface failure.

Misfit dislocations reduce the effective interface area (metal atoms on O site), which ultimately leads to a decrease in $t_{int}^{max}$ compared with ideal interface strength. The dislocation width $w_{dis}$ can be estimated based on the drop of $t_{int}^{max}$[50]

$$t_{semi}^{max} = t_{cohe}^{max}\left(1 - \frac{w_{dis}L}{S}\right)$$

(12)

where $t_{semi}^{max}$ and $t_{cohe}^{max}$ are the tensile strengths of semi-coherent and coherent interfaces, $L$ is the dislocation length, and $S$ is the interface area. In principle, $w_{dis}$ depends on the dislocation distance $w$, interface interaction, and stiffness of the two

constituent materials. The dimensionless dislocation widths $w_{dis}/w$ listed in Table 2 show that the Au/MgO interface has the smallest dislocation width while the Ag/MgO interface has the largest dislocation width, which suggests that the weakening effect of misfit dislocations on the Ag/MgO interface is the most significant.

**4.3. Scale Effects.** As discussed in Section 2, both catastrophe point and spring-back length are scale-dependent. Figure 8 shows the interface traction−separation relationships of both coherent and semi-coherent metal/MgO(001) interfaces with different thicknesses. The thickness ratio between metal and MgO is kept as 1.

For comparison of the results of the spring series model and atomistic simulation method, we calculated the interface displacement at catastrophe point $\delta'_{int}$ and spring-back length $\Delta\delta_{int}$ of three metal/MgO interface systems of different thicknesses, as shown in Table 4. For the thin Au/MgO interface system (4u−4u), due to the relatively low interface strength and soft metal, the elastic energy accumulated in the loading stage is insufficient to break the interface to form two new free surfaces. Therefore, no spring-back occurs during the interface fracture process. For each model thickness, the $\delta'_{int}$ by atomistic simulation is smaller than that of the spring series model, while the $\Delta\delta_{int}$ by atomistic simulation is larger than that of the spring series model. This is mainly due to the boundary effect in atomistic simulations,[43] which causes the atomistic interface model to be stretched to a greater degree than the theoretical model in the loading stage. However, both the theoretical model and atomistic simulation results show a similar effect of model thickness: the thicker the interface model, the closer the catastrophe point is to the peak interface traction, and the longer the spring-back length after interface breaking. For example, with the increase of the model thickness, the interface

displacement at the catastrophe point $\delta'_{int}$ of the Pd/MgO interface in the atomistic simulations decreases from 0.57 to 0.43 Å, while the spring-back length increases from 1.39 to 5.08 Å.

The reasons for the observed effect of thickness are twofold. For the catastrophe point, eq 7 shows that the absolute value of the slope of the interface cohesive curve at the catastrophe point decreases with the increase of model thickness, indicating that the catastrophe point of the thick interface model is close to the peak interface traction where the slope is zero. Therefore, as the model thickness increases, the catastrophe point gradually approaches the peak interface traction from a location after the peak interface traction. For the spring-back length, the length of all interfaces increases as the thickness of the model increases, as indicated by eq 10. Besides, the spring-back length is also material-specific. For the metal/MgO interface system formed by a relatively strong interface and soft metal (e.g., the Ag/MgO interface system), more elastic energy is accumulated in bulk materials during the loading stage. The huge difference in energy distribution between bulk and interface cohesive parts promotes the rapid release of elastic energy, which is macroscopically reflected as a catastrophic failure of the interface and obvious interface spring-back. On the contrary, for the metal/MgO interface system formed by a relatively weak interface (e.g., the Au/MgO interface system), the system stores less elastic energy at the catastrophe point. After interface spring-back, a smaller energy release rate corresponds to a shorter spring-back length, indicating a more continuous interface fracture process.

Figure 8b shows the interface cohesive relationships of the three semi-coherent metal/MgO interface systems with different thicknesses. Similar to the scale effects of coherent interface systems, thicker semi-coherent interface models show more pronounced catastrophic failure characteristics: the catastrophe traction $t^c_{int}$ is closer to the peak interface traction and the spring-back length after interface breaking is longer. On the other hand, the interface fracture processes of semi-coherent interfaces appear to be more continuous. Because of the decreased interface tensile strengths, the spring-back lengths are all about 50% shorter than those of the same thickness coherent interface systems.

## 5. DISCUSSION

In this work, we have characterized the atomic scale catastrophic failure process of metal/ceramic interfaces based on the spring series model and atomistic simulations. We have quantitatively analyzed the material and structure factors that influence the beginning (catastrophe point) and end (spring-back length) of the catastrophic failure process and found that the catastrophe point approaches the peak interface traction as the model thickness increases. Besides, the fracture process of the semi-coherent interface is more continuous than the coherent interface due to the gradual breaking of interface springs.

The interface traction–separation curves of different thickness interface models all fall on the same cohesive curve for a specific interface. This relationship reflects the intrinsic properties of the interface, which depends on the constituent materials and crystal orientation relationship. The area under the traction–separation relationship represents the atomistic scale fracture energy of the interface. To connect the atomistic and engineering descriptions of the cohesive law, Nguyen et al.[16] coarse-grain the cohesive behavior of a cohesive layer by a reduction in the cohesive traction and an increase in the opening displacement range, while the fracture energy remains invariant. Macroscopically, the interface fracture can be regarded as the

cooperative behavior of a large number of interatomic planes. The length of the cohesive zone, which is the distance from the crack tip to the point where the maximum cohesive traction is attained,[51] measures the local element size. Based on the relative magnitude of the fracture energy at the atomic scale ($\Phi_{Pd/MgO} > \Phi_{Ag/MgO} > \Phi_{Au/MgO}$), we preliminarily estimated that the cohesive zone size $l$ of the three interfaces is sorted as $l_{Pd/MgO} > l_{Ag/MgO} > l_{Au/MgO}$, assuming that the macroscopic maximum cohesive traction of the three interfaces do not differ much.

In metal/ceramic layered systems, the metal and ceramic are usually polycrystals. A crack in an interface can experience either kinking or cleaving along the grain boundaries depending mainly on the relative toughness associated with the competing direction of advance.[39] According to Griffith,[52] the mechanical energy release upon crack advance must be in balance with the energy required to create the two new surfaces. Therefore, crystal lattice planes with low surface energies are energetically favored as cleavage planes. To investigate the directional anisotropy of the three fcc-metal/MgO interfaces during fracture, we calculated the interfacial separation energies of three perfect fcc-metal/MgO (110) interfaces. The specific potential parameters can be referred to ref 53. Figure 9 shows the
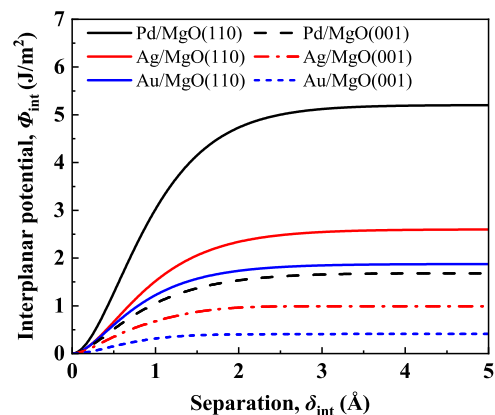


**Figure 9.** Interplanar potentials of fcc-metal/MgO(110) interfaces and fcc-metal/MgO(001) interfaces.

change of system energy relative to the equilibrium interface structure during a rigid-type fracture simulation. The energy required to break the interface is the interfacial separation energy $E_{sep}$, which corresponds to the plateau of the interplanar potential energy curve. For the three fcc-metal/MgO interfaces, the interfacial separation energies of metal/MgO(110) interfaces are all higher than that of the corresponding metal/MgO(001) interfaces, indicating that the metal/MgO(001) interface is energetically favorable for a crack to propagate. The comparative theoretical study of the Ag/MgO(100) and (110) interfaces based on first-principles calculations also showed this directional anisotropy.[54]

For heterogeneous interface systems composed of polycrystalline materials, grain boundaries are also the source of crack initiation and propagation. Intergranular and transgranular microcracking represent two of the main failure mechanisms. For cleavage fracture, where the crack propagation speed is high with negligible or no plastic deformation, the occurrence of the two cracking modes is affected by several factors such as crystallographic lattice, the surface, and the modulus. The spring series model can be extended to grain boundary fracture problems to predict the catastrophic failure behavior of grain

boundaries. On the other hand, to compensate for the mismatch between the orientation of the cleavage planes on either side of the interface, grain boundaries can also provide resistance to cleavage fracture.[55]

## 6. CONCLUSIONS

In this study, the catastrophic failure process of metal/ceramic interfaces was characterized using the spring series model and molecular static simulations. The theoretical catastrophe point at which the interface begins to cleavage fracture falls behind the peak interface traction. The thicker the interface model, the closer the catastrophe point is to the peak interface traction. After the catastrophe point, the interface enters the fast-softening stage and an obvious interface spring-back phenomenon occurs accompanied by a rapid release of elastic energy. The spring-back length, which characterizes the rate of energy release, depends on the catastrophic stress, model thickness, and stiffness of bulk materials. For semi-coherent interfaces with misfit dislocations, the interface strength is reduced by nearly half compared with the ideal strength due to the decrease of an effective interface area. As the model thickness increases, more elastic strain energy is accumulated in bulk materials before fracture and the interface shows catastrophic failure characteristics. This study sheds insight into the mechanisms of cleavage fracture at metal/ceramic interfaces and may help to address the mechanical instability of layered metal—ceramic composites under extreme conditions (low temperature and high loading rate) through material and microstructure design.

## ■ AUTHOR INFORMATION

**Corresponding Authors**

**Lihong Liang** — *College of Mechanical and Electrical Engineering and Beijing Key Laboratory of Health Monitoring and Self-Recovery for High-End Mechanical Equipment, Beijing University of Chemical Technology, Beijing 100029, China*; Email: lianglh@mail.buct.edu.cn

**Yueguang Wei** — *College of Engineering, Peking University, Beijing 100871, China*; Email: weiyg@pku.edu.cn

**Author**

**Xueqiong Fu** — *Shenzhen Institute of Advanced Electronic Materials, Shenzhen Institute of Advanced Technology, Chinese Academy of Sciences, Shenzhen 518055, China*; ● orcid.org/0000-0003-0508-4373

Complete contact information is available at:
https://pubs.acs.org/10.1021/acsomega.2c07953

**Notes**
The authors declare no competing financial interest.

## ■ REFERENCES

(1) Wang, Z.; Schmalbach, K. M.; Penn, R. L.; Poerschke, D.; Antoniou, A.; Mara, N. A.; Stein, A. 3D Periodic and Interpenetrating Tungsten-Silicon Oxycarbide Nanocomposites Designed for Mechanical Robustness. *ACS Appl. Mater. Interfaces* **2021**, *13*, 32126−32135.

(2) Zhu, Q.; Pan, Z.; Zhao, Z.; Cao, G.; Luo, L.; Ni, C.; Wei, H.; Zhang, Z.; Sansoz, F.; Wang, J. Defect-driven selective metal oxidation at atomic scale. *Nat. Commun.* **2021**, *12*, No. 558.

(3) Zhang, Z.; Long, Y.; Cazottes, S.; Daniel, R.; Mitterer, C.; Dehm, G. The peculiarity of the metal-ceramic interface. *Sci. Rep.* **2015**, *5*, No. 11460.

(4) Boissonnet, G.; Bonnet, G.; Pasquet, A.; Bourhila, N.; Pedraza, F. Evolution of thermal insulation of plasma-sprayed thermal barrier coating systems with exposure to high temperature. *J. Eur. Ceram. Soc.* **2019**, *39*, 2111−2121.

(5) Yazdani, A.; Isfahani, T. Hardness, wear resistance and bonding strength of nano structured functionally graded Ni-Al 2 O 3 composite coatings fabricated by ball milling method. *Adv. Powder Technol.* **2018**, *29*, 1306−1316.

(6) Bao, Z.; Guo, X.; Shang, F. An atomistic investigation into the nature of fracture of Ni/Al2O3 interface with yttrium dopant under tension. *Eng. Fract. Mech.* **2015**, *150*, 239−247.

(7) Mishra, A. K.; Gopalan, H.; Hans, M.; Kirchlechner, C.; Schneider, J. M.; Dehm, G.; Jaya, B. N. Strategies for damage tolerance enhancement in metal/ceramic thin films: Lessons learned from Ti/TiN. *Acta Mater.* **2022**, *228*, No. 117777.

(8) Dhariwal, N.; Miraz, A. M.; Meng, W. J.; Ramachandran, B. R.; Wick, C. D. Impact of metal/ceramic interactions on interfacial shear strength: Study of Cr/TiN using a new modified embedded-atom potential. *Mater. Des.* **2021**, *210*, No. 110120.

(9) Wu, Z.; Jiang, X.; Sun, H.; Shao, Z.; Shu, R.; Zhang, Y.; Fang, Y. Nano/micro-scale numerical simulation and microscopic analysis on metal/oxide interfaces: A review. *Composites, Part A* **2022**, *163*, No. 107184.

(10) Ernst, F. Metal-oxide interfaces. *Mater. Sci. Eng. R* **1995**, *14*, 97−156.

(11) Chen, J. H.; Cao, R. Introduction. In *Micromechanism of Cleavage Fracture of Metals*; Chen, J. H.; Cao, R., Eds.; Butterworth-Heinemann: Boston, 2015; Chapter 1, pp 1−54.

(12) Tanguy, D. Cohesive stress heterogeneities and the transition from intrinsic ductility to brittleness. *Phys. Rev. B* **2017**, *96*, No. 174115.

(13) Kwan, M.; Braccini, M.; Jain, A.; Lane, M. W.; Ramanath, G. Interplay between bond breaking and plasticity during fracture at a nanomolecularly-modified metal-ceramic interface. *Scr. Mater.* **2016**, *121*, 42−44.

(14) Jain, A.; Singh, B.; Garg, S.; Ravishankar, N.; Lane, M.; Ramanath, G. Atomistic fracture energy partitioning at a metal-ceramic interface using a nanomolecular monolayer. *Phys. Rev. B* **2011**, *83*, No. 035412.

(15) Barenblatt, G. I. The Mathematical Theory of Equilibrium Cracks in Brittle Fracture. In *Advances in Applied Mechanics*; Dryden, H. L.; von Kármán, T.; Kuerti, G.; van den Dungen, F. H.; Howarth, L., Eds.; Elsevier, 1962; Vol. 7, pp 55−129.

(16) Nguyen, O.; Ortiz, M. Coarse-graining and renormalization of atomistic binding relations and universal macroscopic cohesive behavior. *J. Mech. Phys. Solids* **2002**, *50*, 1727−1741.

(17) Del Piero, G.; Truskinovsky, L. Macro- and micro-cracking in one-dimensional elasticity. *Int. J. Solids Struct.* **2001**, *38*, 1135−1148.

(18) Braides, A.; Maso, G. D.; Garroni, A. Variational formulation of softening phenomena in fracture mechanics: the one-dimensional case. *Arch. Ration. Mech. Anal.* **1999**, *146*, 23−58.

(19) Lazarus, V.; Buchholz, F. G.; Fulland, M.; Wiebesiek, J. Comparison of predictions by mode II or mode III criteria on crack front twisting in three or four point bending experiments. *Int. J. Fract.* **2008**, *153*, 141−151.

(20) Ghanekar, P.; Kubal, J.; Cui, Y. R.; Mitchell, G.; Delgass, W. N.; Ribeiro, F.; Greeley, J. Catalysis at Metal/Oxide Interfaces: Density Functional Theory and Microkinetic Modeling of Water Gas Shift at Pt/MgO Boundaries. *Top. Catal.* **2020**, *63*, 673−687.

(21) Zhao, Z. J.; Li, Z. L.; Cui, Y. R.; Zhu, H. Y.; Schneider, W. F.; Delgass, W. N.; Ribeiro, F.; Greeley, J. Importance of metal-oxide interfaces in heterogeneous catalysis: A combined DFT, microkinetic, and experimental study of water-gas shift on Au/MgO. *J. Catal.* **2017**, *345*, 157−169.

(22) Ling, S. L.; Watkins, M. B.; Shluger, A. L. Effects of Oxide Roughness at Metal Oxide Interface: MgO on Ag(001). *J. Phys. Chem. C* **2013**, *117*, 5075−5083.

(23) Yang, X. H.; Gu, Y. S.; Migliorato, M.; Zhang, Y. Impact of insulator layer thickness on the performance of metal-MgO-ZnO tunneling diodes. *Nano Res.* **2016**, *9*, 1290−1299.

(24) Matsunaka, D.; Shibutani, Y. Electronic states and adhesion properties at metal/MgO incoherent interfaces: First-principles calculations. *Phys. Rev. B* **2008**, *77*, No. 165435.

(25) You, X. M.; Liang, L. H.; Wei, Y. G. The atomistic simulation study of Ag/MgO interface tension fracture. *Comput. Mater. Sci.* **2018**, *142*, 277−284.

(26) Finnis, M. W. The theory of metal - ceramic interfaces. *J. Phys.: Condens. Matter* **1996**, *8*, 5811−5836.

(27) Renaud, G.; Guenard, P.; Barbier, A. Misfit dislocation network at the Ag/MgO (001) interface: a grazing-incidence x-ray-scattering study. *Phys. Rev. B* **1998**, *58*, 7310−7318.

(28) Vitek, V.; Gutekunst, G.; Mayer, J.; Rühle, M. Atomic structure of misfit dislocations in metal-ceramic interfaces. *Philos. Mag. A* **1995**, *71*, 1219−1239.

(29) Pauwels, B.; Van Tendeloo, G.; et al. Low-energy-deposited Au clusters investigated by high-resolution electron microscopy and molecular dynamics simulations. *Phys. Rev. B* **2000**, *62*, 10383−10393.

(30) Renaud, G.; Barbier, A.; Robach, O. Growth, structure, and morphology of the Pd/MgO(001) interface: Epitaxial site and interfacial distance. *Phys. Rev. B* **1999**, *60*, 5872−5882.

(31) Chen, D.; Ma, X. L.; Wang, Y. M. First-principles study of the interfacial structures ofAu/MgO(001). *Phys. Rev. B* **2007**, *75*, No. 125409.

(32) Ouahab, A.; Mottet, C.; Goniakowski, J. Atomistic simulation of Ag thin films on MgO(100) substrate: A template substrate for heterogeneous adsorption. *Phys. Rev. B* **2005**, *72*, No. 035421.

(33) Vervisch, W.; Mottet, C.; Goniakowski, J. Theoretical study of the atomic structure of Pd nanoclusters deposited on a MgO(100) surface. *Phys. Rev. B* **2002**, *65*, No. 245411.

(34) Long, Y.; Chen, N. X.; Zhang, W. Q. Pair potentials for a metal−ceramic interface by inversion of adhesive energy. *J. Phys.: Condens. Matter* **2005**, *17*, 2045−2058.

(35) Fu, X. Q.; Liang, L. H.; Wei, Y. G. Atomistic simulation study on the shear behavior of Ag/MgO interface. *Comput. Mater. Sci.* **2018**, *155*, 116−128.

(36) Meltzman, H.; Mordehai, D.; Kaplan, W. D. Solid−solid interface reconstruction at equilibrated Ni−Al2O3 interfaces. *Acta Mater.* **2012**, *60*, 4359−4369.

(37) Plimpton, S. Fast Parallel Algorithms for Short-Range Molecular Dynamics. *J. Comput. Phys.* **1995**, *117*, 1−19.

(38) M, L.; Bass, H. E.; Stern, R. R. *Handbook of Elastic Properties of Solids Liquids and Gases*; Academic Press: New York, 2001; Vol. *2*.

(39) Hutchinson, J. W.; Suo, Z. Mixed Mode Cracking in Layered Materials. *Adv. Appl. Mech.* **1991**, *29*, 63−191.

(40) Parry, G.; Coupeau, C.; Colin, J.; Cimetière, A.; Grilhé, J. Buckling and post-buckling of stressed straight-sided wrinkles: experimental AFM observations of bubbles formation and finite element simulations. *Acta Mater.* **2004**, *52*, 3959−3966.

(41) Zak, S.; Lassnig, A.; Hrstka, M.; Cordill, M. J. Buckling-induced delamination: Connection between mode-mixity and Dundurs parameters. *Theor. Appl. Fract. Mech.* **2022**, *122*, No. 103647.

(42) Dundurs, J. Effect of elastic constants on stress in a composite under plane deformation. *J. Compos. Mater.* **1967**, *1*, 310−322.

(43) Zhang, X.; Zhang, B.; Mu, Y.; Shao, S.; Wick, C. D.; Ramachandran, B. R.; Meng, W. J. Mechanical failure of metal/ceramic interfacial regions under shear loading. *Acta Mater.* **2017**, *138*, 224−236.

(44) Lu, P.; Cosandey, F. Electron microscopy studies of metal/MgO interfaces. *Ultramicroscopy* **1992**, *40*, 271−280.

(45) Lu, P.; Cosandey, F. Dislocation structures at CuMgO and PdMgO interfaces. *Acta Metall. Mater.* **1992**, *40*, S259−S266.

(46) Benedek, R.; Minkoff, M.; Yang, L. H. Adhesive energy and charge transfer for MgO/Cu heterophase interfaces. *Phys. Rev. B* **1996**, *54*, 7697−7700.

(47) Robach, O.; Renaud, G.; Barbier, A. Structure and morphology of the Ag/MgO(001) interface during in situ growth at room temperature. *Phys. Rev. B* **1999**, *60*, 5858−5871.

(48) Stankic, S.; Cortes-Huerto, R.; Crivat, N.; Demaille, D.; Goniakowski, J.; Jupille, J. Equilibrium shapes of supported silver clusters. *Nanoscale* **2013**, *5*, 2448−2453.

(49) Trampert, A.; Ernst, F.; Flynn, C. P.; Fischmeister, H. F.; Ruhle, M. High-resolution transmission electron-microscopy studies of the Ag/MgO interface. *Acta Metall. Mater.* **1992**, *40*, S227−S236.

(50) Long, Y.; Chen, N. X. Theoretical study of misfit dislocation in interface dynamics. *Comput. Mater. Sci.* **2008**, *44*, 721−727.

(51) Turon, A.; Dávila, C. G.; Camanho, P. P.; Costa, J. An engineering solution for mesh size effects in the simulation of delamination using cohesive zone models. *Eng. Fract. Mech.* **2007**, *74*, 1665−1682.

(52) Griffith, A. A. The Phenomena of Rupture and Flow in Solids. *Philos. Trans. R. Soc. A* **1920**, *A221*, 163−198.

(53) Chen, J.; Chen, N. Theoretical study of fcc-metal/MgO(110) interfacial potentials. *J. Phys.: Condens. Matter* **2010**, *22*, No. 215001.

(54) Zhukovskii, Y. F.; Kotomin, E. A.; Jacobs, P. W. M.; Stoneham, A. M.; Harding, J. H. Comparative theoretical study of the Ag−MgO (100) and (110) interfaces. *Surf. Sci.* **1999**, *441*, 373−383.

(55) Hughes, G. M.; Smith, G.; Crocker, A. G.; Flewitt, P. E. J. An examination of the linkage of cleavage cracks at grain boundaries. *Mater. Sci. Technol.* **2005**, *21*, 1268−1274.